Monthly Notices
of the
ROYAL ASTRONOMICAL SOCIETY

MNRAS **464,** 3871–3881 (2017)
Advance Access publication 2016 October 12

doi:10.1093/mnras/stw2628

Testing multimass dynamical models of star clusters with real data: mass segregation in three Galactic globular clusters

A. Sollima,[1,2]★ E. Dalessandro,[1,2] G. Beccari[3] and C. Pallanca[2]

[1]*INAF Osservatorio Astronomico di Bologna, via Ranzani 1, Bologna I-40127, Italy*
[2]*Dipartimento di Astronomia, Universitá di Bologna, via Ranzani 1, Bologna I-40127, Italy*
[3]*European Southern Observatory, Karl-Schwarzschild-Strasse 2, D-85748 Garching bei Munchen, Germany*

Accepted 2016 October 11. Received 2016 October 7; in original form 2016 August 6; Editorial Decision 2016 October 7

ABSTRACT

We present the results of the analysis of deep photometric data for a sample of three Galactic globular clusters (NGC5466, NGC6218 and NGC 6981) with the aim of estimating their degree of mass segregation and testing the predictions of analytic dynamical models. The adopted data set, composed of both *Hubble Space Telescope* and ground-based data, reaches the low-mass end of the mass functions of these clusters from the centre up to their tidal radii allowing us to derive the radial distribution of stars with different masses. All the analysed clusters show evidence of mass segregation with the most massive stars being more concentrated than the low-mass ones. The structures of NGC5466 and NGC6981 are well reproduced by multimass dynamical models adopting a lowered Maxwellian distribution function and the prescription for mass segregation given by Gunn & Griffin. Instead, NGC6218 appears to be more mass segregated than model predictions. By applying the same technique to mock observations derived from snapshots selected from suitable *N*-body simulations, we show that the deviation from the behaviour predicted by these models depends on the particular stage of dynamical evolution regardless of initial conditions.

Key words: methods: data analysis – methods: observational – techniques: photometric – stars: luminosity function, mass function – stars: Population II – globular clusters: individual: NGC5466, NGC6218, NGC6981.

1 INTRODUCTION

The dynamical evolution of globular clusters (GCs) is one of the most intriguing topics of stellar astrophysics. Indeed, GCs are stellar systems composed of billions of stars subject to their mutual gravitational attraction being the best representation in nature of the 'gravitation *N*-body problem'. Moreover, since GCs are the oldest stellar systems known, their half-mass relaxation time is often shorter than their ages, and processes like kinetic energy equipartition, mass segregation and core collapse can be at work and leave signatures in the phase-space distribution of their stars.

Stars in GCs cover a wide range of masses from $\sim 0.1\,M_{\odot}$ [the faintest main-sequence (MS) stars] to $>14\,M_{\odot}$ (the heaviest black holes; Belczynski et al. 2010) with a distribution which varies from cluster to cluster and is generally bottom-heavy (with a larger number of low-mass stars than high-mass ones; Paust et al. 2010). Because of the cumulative effect of many long-range two-body encounters, stars with high kinetic energies (i.e. massive and/or fast) transfer energy to less energetic (low-mass and/or slow) ones. As a consequence, high-mass stars sink towards less energetic orbits preferentially located in the innermost cluster region, while low-mass stars diffuse in an extended halo. So, the variation of the density and velocity dispersion distribution across the cluster extent correlated with stellar mass represents the most direct evidence of dynamically evolution of a star cluster.

Observational evidence of mass segregation has been shown for many GCs using, as a benchmark, the radial variation of the mass function (MF; Da Costa 1982; Irwin & Trimble 1984; Pryor, Smith & McClure 1986; Richer, Fahlman & Vandenberg 1988; Bolte 1989; Fahlman, Richer & Nemec 1991; Drukier et al. 1993; Paresce, de Marchi & Jedrzejewski 1995; De Marchi & Paresce 1996; Ferraro et al. 1997; Zaggia, Piotto & Capaccioli 1997; Fischer et al. 1998; Rosenberg et al. 1998; Saviane et al. 1998; Rood et al. 1999; Andreuzzi et al. 2000, 2004; Albrow, De Marchi & Sahu 2002; Lee et al. 2003, 2004; Koch et al. 2004; Pasquali et al. 2004; Balbinot et al. 2009; Pasquato et al. 2009; Beccari et al. 2010; Goldsbury, Heyl & Richer 2013; Frank, Grebel & Küpper 2014; Martinazzi et al. 2014; Zhang et al. 2015) or the radial distribution of massive objects like blue straggler stars and/or binaries (Ferraro et al. 2012 and references therein; Dalessandro et al. 2015).

On the other hand, kinematic evidence of energy exchange between mass groups represents an observational challenge because of the prohibitive performances required to extract accurate kinematics

★ E-mail: antonio.sollima@oabo.inaf.it

for large samples of GC stars in a significant range of magnitudes along the MS. Indeed, radial velocities have been obtained essentially only for the brightest stars, giants and subgiants, which have very similar masses. To date, the measure of a significant number of radial velocities for stars in a range of masses has been performed through integral field spectroscopy only in the GC NGC 6397, leading however to uncertain results (Kamann et al. 2016). The same kind of analysis made through proper motions requires superb astrometric accuracies that have been achieved only recently using *Hubble Space Telescope (HST)* multi-epoch observations providing evidence for mass-dependent kinetic temperature in M15 (Bellini et al. 2014).

The presence and degree of mass segregation affect the determination of many cluster structural parameters like mass, size, MF and mass-to-light ratio. These quantities are indeed estimated using information coming from the brightest (relatively massive) stars for which kinematics are available and contributing to the large majority of the cluster light, and later corrected using the predictions of dynamical models.

The most direct way to model the dynamical evolution of a stellar system is through the use of *N*-body simulations. However, in spite of the impressive progress of the computing power in the last decades, the fit of star cluster observables with direct *N*-body simulations has been feasible only for open cluster-like objects (Hurley et al. 2005; Harfst, Portegies Zwart & Stolte 2010) or small GCs (Zonoozi et al. 2011, 2014; Heggie 2014; Wang et al. 2016). This is because a single simulation with a number of particles consistent with that observed in GCs (10^{5-6}) requires months of computing time, and a large number of simulations are needed to tune the initial conditions in a similar way to reproduce, after a Hubble time, the present-day structure and properties of a given GC. Similarly, Monte Carlo simulations, although providing a significant improvement in speed, are subject to the same limitation (Giersz 2006; Giersz, Heggie & Hurley 2008; Giersz & Heggie 2009, 2011).

An alternative way to model the structure of a multimass stellar system is the use of analytic models. Analytic models are generally defined by distribution functions depending on constants of the motion, and assume that the cluster is in a steady state and in equilibrium with the surrounding tidal field. Because star clusters are collision-dominated systems, we have a relatively advanced understanding of the distribution of their stars in phase space from theory and numerical simulations, and the choice of distribution-function-based models is justified. The most popular model of this kind is the King (1966) model, which proved to be quite effective in reproducing the surface brightness profiles of many GCs, open clusters and dwarf galaxies (Djorgovski 1993; McLaughlin & van der Marel 2005; Carballo-Bello et al. 2012; Miocchi et al. 2013). A generalization of this model accounting for radial anisotropy and a degree of equipartition among an arbitrary number of mass components has been provided by Gunn & Griffin (1979; see also Da Costa & Freeman 1976; Merritt 1981). The underlying assumptions of these models (i.e. the functional dependence of the distribution function on the integrals of motion and masses), although relying on a physical basis, are only arbitrary guesses to model the result of the complex interplay among many physical processes. It is therefore essential to test the predictions of these models with suitable sets of observational data.

Since the first observational evidence of mass segregation in GCs, the prediction of analytic multimass models has been compared with observations, providing generally good results (Richer & Fahlman 1989; King, Sosin & Cool 1995; Sosin 1997; Richer et al. 2004; Beccari et al. 2015). However, these studies consist mainly of only two pointings at different distances from the cluster centre and sample a small portion of the cluster MF. In the absence of suitable observational data, recent studies tested the prediction of analytical models using snapshots extracted from the sets of numerical simulations. In this regard, Takahashi & Lee (2000) fitted the outcome of the Fokker–Planck simulations including the effect of an external tidal field and anisotropy with multimass King–Michie models and found that although they provide a reasonable fit of the more massive components, they underestimate two-body relaxation effects for low-mass stars leading to significant biases in the conversion between local and global MFs. Trenti & van der Marel (2013) noted that the simulated clusters never reach complete kinetic energy equipartition [confirming what already found by Inagaki & Saslaw (1985) and Baumgardt & Makino (2003) through Fokker–Planck and *N*-body simulations] and argued that the widely used King–Michie models could be inadequate to model these stellar systems. In Sollima et al. (2015), the biases in the estimation of the mass and MF of two *N*-body simulations have been quantified by adopting different fitting techniques employing multimass King–Michie models. In this work, we found that these quantities are correctly estimated (within ∼10 per cent) during the cluster evolution after the first half-mass relaxation time.

In this paper, we present an in-depth analysis of the radial distribution of stars in a relatively wide range of masses in three Galactic GCs, namely NGC 5466, NGC 6218 and NGC 6981. The aim of this work is to quantify the accuracy of multimass models in reproducing the degree of mass segregation measured in these GCs. In Section 2, we describe the adopted photometric data set together with the observational strategy and reduction technique. Section 3 is devoted to the description of the fitting algorithm. The results of the application of the adopted technique to a set of *N*-body simulations and the comparison with observations are shown in Section 4. Finally, we summarize our results in Section 5.

2 OBSERVATIONAL MATERIAL

The main photometric data base used to sample the central part of all the target GCs is constituted by the set of publicly available deep photometric catalogues of the 'globular cluster treasury project' (Sarajedini et al. 2007). It consists of high-resolution *HST* images secured with the Advanced Camera for Surveys (ACS) Wide Field Channel through the *F606W* and *F814W* filters. The field of view of the camera (202 arcsec × 202 arcsec) is centred on the clusters' centre with a dithering pattern to cover the gap between the two chips, allowing a full coverage of the core of the GCs considered in our analysis. This survey provides deep colour–magnitude diagrams (CMDs) reaching the faint MS of the target clusters down to the hydrogen burning limit (at $M_V \sim 10.7$) with a signal-to-noise ratio of S/N > 10. The results of artificial star experiments are also available to allow an accurate estimate of the completeness level and photometric errors. A detailed description of the photometric reduction, astrometry and artificial star experiments can be found in Anderson et al. (2008).

The outer region of NGC 5466 has been analysed using images collected with the Large Binocular Camera (LBC) mounted at the Large Binocular Telescope (Mount Graham, Arizona) while for the other two GCs the FOcal Reducer and low dispersion Spectrograph 2 (FORS2) camera at the Very Large Telescope of the European Southern Observatory (Cerro Paranal, Chile) has been used. Maps of the ACS, LBC and FORS2 pointings across the GCs' field of view are shown in Fig. 1.

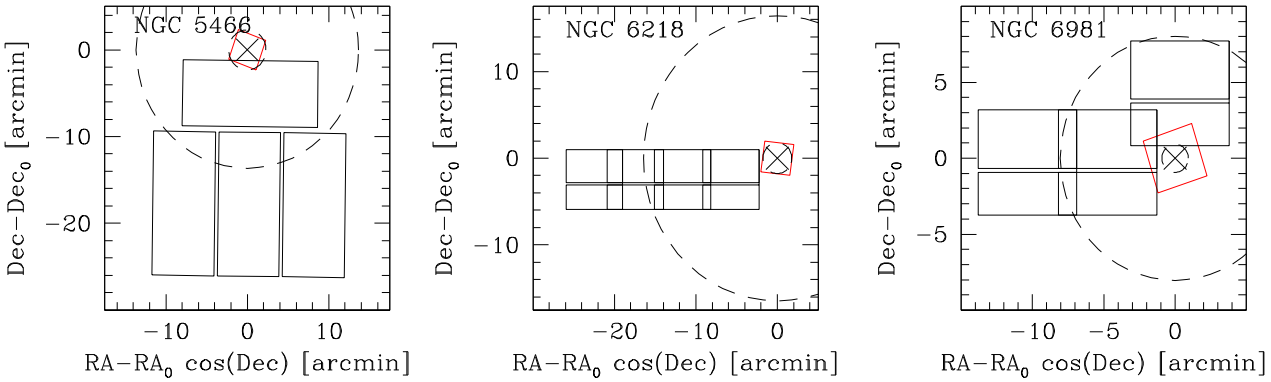

Figure 1. Maps of the region sampled by our observations. The ACS and ground-based pointings are marked with red (grey in the printed version of the paper) and black lines, respectively. The cluster centre, the half-light and the tidal radii derived by McLaughlin & van der Marel (2005) are shown as dashed lines.

Table 1. Observing logs.

Name	Instrument	Filter	Exp. time (s)	No. of exp. per field
NGC 5466	LBC	*B*	5	1
		B	90	7
		B	400	11
		V	5	1
		V	60	7
		V	200	15
NGC 6218	FORS2	*V*	165	15
		I	105	12
NGC 6981	FORS2	*V*	515	8
		I	240	16

The LBC is a wide-field imager which provides an effective 23 arcmin × 23 arcmin field of view, sampled at 0.224 arcsec pixel^{-1} over four chips of 2048×4608 pixels each. Observations were performed in a photometric night (2010 April 11) using the blue detector of the LBC camera. A set of short exposures was secured in the *B* and *V* filters with the cluster centre positioned in the central chip of the LBC-blue CCD mosaic. Deep images were obtained with the LBC-blue's field of view positioned ∼100 arcsec south from the cluster centre. This data set has been recently used to derive the radial distribution of blue stragglers and binaries as well as the MF of NGC 5466 (Beccari et al. 2013, 2015).

The FORS2 camera has been used with the standard resolution collimator providing a pixel scale of 0.25 arcsec pixel^{-1} and a field size of 6.8 arcmin × 6.8 arcmin. A set of deep *V* and *I* images has been secured in a mosaic pattern allowing us to reach the nominal tidal radii of the observed clusters. Raw images were corrected for bias and flat-field, and the overscan region was trimmed using the standard IRAF tasks.

The average seeing was comprised in the interval of 0.5–1.0 arcsec and remained stable within 0.2 arcsec during each observing night so that all the images of both data sets were used in the photometric analysis. A log of the observations is listed in Table 1.

The raw LBC and FORS2 frames were corrected for bias and flat-fields and the overscan region was trimmed using LBC Survey data centre pipeline and the IRAF[1] task *imred*, respectively. The photometric reduction of both data sets has been performed using the DAOPHOT/ALLFRAME point spread function (PSF)-fitting routine (Stetson 1994). Images were aligned and corrected for geometric distortion using a third-order polynomial. We performed the source detection on the stack of all images while the photometric analysis was performed independently on each undistorted image. Only stars detected in two out of three long exposures or in the short ones have been included in the final catalogue. We used the most isolated and brightest stars in the field to construct a PSF which has been modelled as a Moffat function plus a numerical component which varies quadratically across the field of view. The same PSF stars were also employed to link the aperture magnitudes to the instrumental ones (a single magnitude shift has been calculated for each chip). Instrumental magnitudes have been then transformed into the standard Johnson–Cousin photometric system using a first-order (zero-point + colour term) linear relation obtained by comparing the stars in common with the standard fields by Stetson.[2] The final catalogues have been astrometrically calibrated through a cross-correlation with the Two Micron All Sky Survey catalogue (Skrutskie et al. 2006). The astrometric solution has a typical standard deviation of 200 mas. A detailed description of the photometric reduction procedure can be found in Beccari et al. (2013) for the LBC data and in a forthcoming paper (Dalessandro et al., in preparation) for the FORS2 ones.

The final CMDs sample the entire unevolved population of the analysed clusters down to ∼7 mag below the turn-off (see Fig. 2). Artificial star experiments have been performed using the procedure described in Bellazzini et al. (2002). A list of input positions and magnitudes has been produced by distributing artificial stars in random positions within a grid of cells (one star per cell) homogeneously distributed across the field of view. The *V* magnitude of artificial stars has been extracted from a power-law distribution with an index $x = -2$ while their colours have been obtained by interpolating them on the cluster ridge line. Artificial stars have been then added to the science frames using the corresponding PSF. The photometric analysis has been then repeated using the same procedure adopted for the science frames producing a catalogue of output positions and magnitudes for artificial stars. At the end of the above procedure, a catalogue of 100 000 artificial stars has been produced allowing a proper estimate of the photometric

[1] IRAF is distributed by the National Optical Astronomy Observatories, which are operated by the Association of Universities for Research in Astronomy, Inc., under cooperative agreement with the National Science Foundation.

[2] http://www.cadc-ccda.hia-iha.nrc-cnrc.gc.ca/en/community/STETSON/standards/

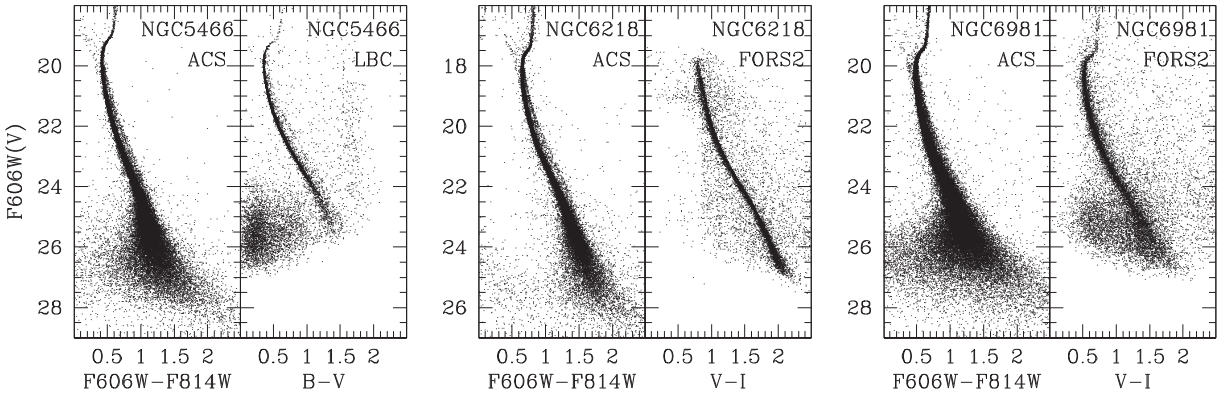

Figure 2. CMDs of the three analysed GCs. In each panel, both the ACS (left inset) and ground based data (right inset) are shown.

accuracy and the completeness level at different magnitudes across the observed field of view.

3 METHOD

We tested the agreement between King–Michie analytic models and observations by comparing the distribution of star masses as a function of projected distances from the cluster centre. In the following sections, we describe the technique adopted to derive masses from our photometric data set as well as the adopted models and the fitting algorithm.

3.1 Stellar masses estimate

GC stars occupy different regions of the CMD according to their evolutionary stages and masses, so an estimate of their masses can be made by means of the comparison with suitable theoretical isochrones. We adopted the theoretical isochrones by Dotter et al. (2007) with metallicity [Fe/H] = −2.31, −1.33 and −1.48 (for NGC5466, NGC6218 and NGC6981, respectively; Carretta et al. 2009) and appropriate ages chosen by best fitting the morphology of the turn-off region of the observed CMD (13.2, 13 and 12.3 Gyr, respectively, in agreement with those estimated by Dotter et al. 2010). Absolute magnitudes have been converted into the observational colour–magnitude plane assuming the distance moduli and reddening listed in the Harris catalogue (Harris 1996; 2010 edition).

This task is however complicated by the contamination from fore/background field stars and by the effect of unresolved binaries and photometric errors spreading out stars far from their original location in the CMD, making it difficult to assign them a proper mass. Although it is not possible to unambiguously distinguish binaries, single and field stars across the entire CMD, we adopt a statistical classification of cluster members. In particular, we adopted the following procedure:

(i) The field of view of the photometric data has been divided into annular concentric regions. We defined 16 regions with both width and separation of 0.1 arcmin in the ACS field of view and 8 regions separated by logarithmic steps of 0.1 starting from 3 arcmin for the ground-based data.

(ii) For each region, a synthetic CMD (containing $\sim 10^6$ stars) has been simulated by randomly extracting masses from a power-law MF and derived the corresponding magnitudes by interpolating through the adopted isochrone. A population of binaries has also been simulated by associating with a fraction of stars a secondary component whose mass has been randomly extracted assuming a flat mass ratio distribution (Milone et al. 2012). The fluxes of the two components have been then summed in both passbands to derive their corresponding magnitudes and colours. A synthetic population of field stars has been also added using the Galactic model by Robin et al. (2003) whose magnitudes have been converted into the ACS photometric system using the transformations by Sirianni et al. (2005).

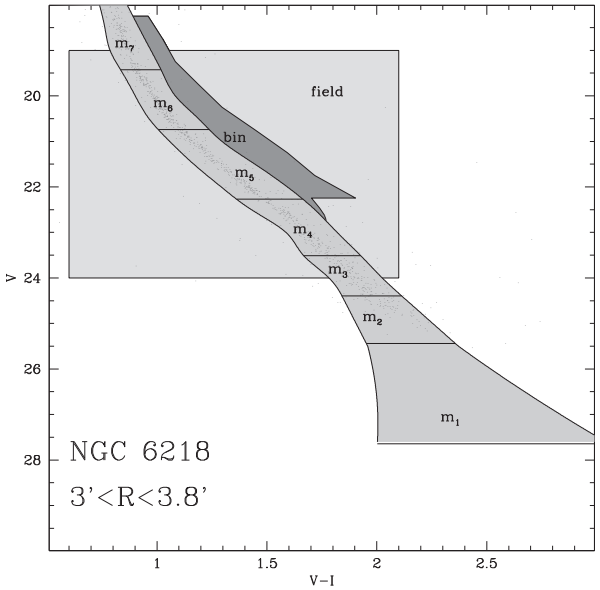

Figure 3. Selection boxes adopted for the population of single stars (m_1 to m_7), binaries (bin) and field stars (field) of NGC 6218. The (V, $V-I$) CMD is overplotted.

In each annulus, the MF slope, the binary fraction and the number of field stars have been tuned to reproduce the observed relative ratios of number counts in nine regions of the CMD defined as follows (see Fig. 3):

(a) Seven V (*F606W*) magnitude intervals were defined corresponding to equal-mass intervals and including all stars with colours within three times the photometric errors corresponding to their magnitudes.

(b) A region including the bulk of the binary populations with high-mass ratios ($q > 0.5$). This last region is delimited in magnitudes by the loci of binaries with primary star mass $M_1 = 0.45\,M_\odot$ (faint boundary) and $M_1 = 0.75\,M_\odot$ (bright boundary), and in colour by the MS ridge line (blue boundary) and the equal-mass

binary sequence (red boundary), both redshifted by three times the photometric error;

(c) A region including mainly field stars in a magnitude interval between 1 and 5 mag in the V band below the turn-off and within the colour range $0.6 < V - I < 2.1$.

(iii) For each synthetic star, a particle in the same radial range and with magnitudes within 0.25 mag has been extracted from the library of artificial stars and, if recovered,[3] the magnitude and colour shift with respect to its input quantities has been added to those of the corresponding star.

(iv) As a final step, we associated with each observed star the mass and the classification flag (single, binary or field contaminant) of the closest particle in the synthetic CMD.

We limited our analysis to stars fainter than the turn-off since in the ground-based data set most of the bright stars belonging to the evolved population saturate in the deep exposures. These objects constitute less than 5 per cent of the total cluster population, so their exclusion does not affect the results of the present analysis.

3.2 Analytic models

We fitted our data set with a set of King–Michie analytic models (Gunn & Griffin 1979). These models are constructed from a lowered Maxwellian distribution function made by the contributions of H mass groups:

$$f(E, L) = \sum_{j=1}^{H} k_j f_j(E, L, m_j),$$

$$f_j(E, L, m_j) = \exp\left(-\frac{A_j L^2}{2\sigma_K^2 r_a^2}\right)\left[\exp\left(-\frac{A_j E}{\sigma_K^2}\right) - 1\right],$$

where E and L are, respectively, the energy and angular momentum per unit mass, r_a is the radius beyond which orbits become biased towards the radial direction, A_j and k_j are scale factors for each mass group and σ_K is a normalization term. Although the distribution function defined above allows for various levels of radial anisotropy, we used only isotropic models for our comparison (assuming $r_a = +\infty$). This is because (i) the presence of a significant degree of velocity anisotropy cannot be verified without a large set of kinematic data (see e.g. Watkins et al. 2015) and (ii) the mass dependence of anisotropy in these models is oversimplified and it does not properly reproduce the behaviour evidenced in N-body simulations in many stages of their evolution (Sollima et al. 2015). The dependence on mass of the coefficients A_j determines the degree of mass segregation of the cluster. In the formulation by Gunn & Griffin (1979), $A_j \propto m_j$ which implies that more massive stars are kinematically colder than less massive ones. Under these assumptions, the distribution function of each mass group is uniquely a function of energy and can be written as a function of the distance from the centre, the velocity and the star mass:

$$f_j(v, r, m_j) = \exp\left(-\frac{m_j v^2}{2m_K\sigma_K^2} - \frac{m_j \psi(r)}{m_K \sigma_K^2}\right) - 1, \quad (1)$$

where ψ is the effective potential defined as the difference between the cluster potential ϕ at a given radius r and the potential at the cluster tidal radius ($\psi \equiv \phi - \phi_t$) and m_K is an arbitrary constant with the dimension of a mass.

The 3D number density of each mass group is obtained by integrating equation (1) over the velocity domain:

$$\rho_j(r) = \int_0^{\sqrt{-2\psi(r)}} 4\pi v^2 k_j f_j(v, r, m_j)\,\mathrm{d}v,$$

$$\rho(r) = \sum_{j=1}^{H} \rho_j(r), \quad (2)$$

while the potential at each radius is determined by the Poisson equation

$$\nabla^2\psi = 4\pi G\rho. \quad (3)$$

Equations (2) and (3) have been integrated after assuming, as a boundary condition, a value of the potential and its derivative at the centre ($\psi_0; \mathrm{d}\psi/\mathrm{d}r(0) = 0$) outward till the radius r_t at which both density and potential vanish (see Gunn & Griffin 1979 and Sollima et al. 2015 for a detailed derivation of the model properties).

Note that the MF is univocally linked to the k_j coefficients, since the number of stars in a given mass bin is given by

$$N_j = 16\pi^2 k_j \int_0^{r_t} r^2 \int_0^{\sqrt{-2\psi(r)}} v^2 f_j(v, r, m_j)\,\mathrm{d}v\,\mathrm{d}r.$$

So, the shape of the density profiles is completely determined by the parameters (ψ_0, N_j) while the constant $m_K\sigma_K^2$ determines the mass of the model and the core radius $r_c \equiv \sqrt{\frac{9\sigma_K^2}{4\pi G\rho_0}}$ describes the size of the system.

As a last step, the above profiles have been projected on to the plane of the sky to obtain the surface density of each bin:

$$\Gamma_j(m_j, R) = 2\int_R^{r_t} \frac{\rho_j r}{\sqrt{r^2 - R^2}}\,\mathrm{d}r.$$

Here, we considered seven evenly spaced mass bins ranging from 0.1 $M_\odot$ to the mass at the red giant branch tip (M_{tip}), plus an additional bin containing all the stellar objects more massive than M_{tip} (like heavy binaries and white dwarfs).

3.3 Fitting algorithm

The best-fitting model has been chosen as the one providing the largest value of the merit function defined as follows:

$$L = \sum_{i=1}^{N_s} \log[P(m_i, R_i)], \quad (4)$$

where N_s is the total number of stars flagged as singles; and $P(m_i, R_i)$ is the probability density to find a single star with mass m_i at a projected distance R_i from the cluster centre according to a given model. This last quantity can be calculated as

$$P(m_i, R_i) = \frac{R_i\ X_s(m_i, R_i)}{\sum_{j=1}^{H} \mu_s(m_j)\,\Delta m \int_0^{R_{max}} R\ X(m_j, R)\,\mathrm{d}R}$$

and

$$X_s(m, R) = \mu_s(m)\,\Gamma(m, R)\,C_s(m, R)\,A(R), \quad (5)$$

where $C_s(m, R)$ is the mean completeness estimated for stars with mass m at a projected distance R from the cluster centre, $A(R)$ is the azimuthal coverage of the observational field of view at a given projected distance, $\mu_s(m)$ is the fraction of single stars with a given mass, Δm is the mass spacing between the model bins and R_{max} is the maximum distance where the fit is performed.

[3] An artificial star has been considered recovered if its input and output magnitudes differ by less than 2.5 log(2) (∼0.75) mag in both *F606W* and *F814W* magnitudes.

The completeness factor as a function of mass and distance $C(m, R)$ has been calculated for both singles and binaries by estimating the V and I magnitudes corresponding to the given mass. We adopted the mass–luminosity relation of the best-fitting isochrone for single stars while for binaries the average magnitudes are calculated from the synthetic CMD simulated as described in Section 3.1. The completeness has been then calculated as the fraction of recovered stars in the artificial star catalogue with input magnitudes within 0.25 mag in both bands and in a distance range within 0.05 arcmin from the given projected radius.

The function $\mu_s(m)$ allows us to account for the population of binaries and of dark remnants contributing to the mass budget of the cluster but not contained in our sample. This parameter is defined as

$$\mu_s(m) \equiv 1 - \mu_{remn}(m) - \mu_b(m), \quad (6)$$

where $\mu_b(m)$ and $\mu_{remn}(m)$ are the fractions of binaries and remnants at a given mass, respectively. These quantities have been calculated in each step of the fitting algorithm (see below) starting from assumptions on the global binary fraction (f_b) and the MF slope (α). In particular,

(i) We simulated a synthetic population of stars extracted from a Kroupa (2001) MF between 0.1 and 8 $M_\odot$.

(ii) We simulated a population of binaries by associating with a fraction f_b of these stars a companion star extracted from a flat distribution of mass ratios.

(iii) We evolved passively all stars (singles and binaries) using the prescriptions of Kruijssen (2009). Because of the upper limit of the adopted initial MF, no neutron stars and black holes are present, consistently with the expectation that they are ejected at birth in these low-mass stellar systems (Kruijssen 2009).

(iv) A fraction of stars are removed as a function of their mass to simulate the effect of evaporation. We assumed that stars evaporate with efficiencies which are a function of their masses only, and are set by the ratio of the present-day MF and the Kroupa (2001) initial MF. For this purpose, a random number ϵ has been extracted from a uniform distribution between 0 and 1, and the star is retained if $\epsilon < \mathrm{Ret}(M)$ where

$$\mathrm{Ret}(M) = \begin{cases} \left(\frac{M_{tip}}{0.5M_\odot}\right)^{\alpha-2.3} \left(\frac{M}{0.5M_\odot}\right)^{1.3-\alpha} & \text{if } M \le 0.5M_\odot, \\ \left(\frac{M}{M_{tip}}\right)^{2.3-\alpha} & \text{if } 0.5\,M_\odot < M \le M_{tip}, \\ 1 & \text{if } M > M_{tip}. \end{cases}$$

(v) The values of μ_s, μ_{bin} and μ_{remn} have been calculated as the fractions of singles, binaries and remnants in the final population in different mass bins.

We set the value of R_{max} to the distance where a power-law density profile starts to develop. This feature is in fact a consequence of deviation from equilibrium occurring because of the interaction with the Milky Way tidal field (Johnston, Sigurdsson & Hernquist 1999; Testa et al. 2000; Küpper et al. 2010) and cannot be properly accounted by King–Michie models assuming equilibrium a priori.

To search the best model in reproducing the distribution of stars in the (m, R) plane, an iterative algorithm has been employed. We start from an initial guess of the MF (through the coefficients N_j) and of the global binary fraction f_b, and repeated the following step until convergence:

Table 2. Parameters of the best-fitting models.

Name	$\log(M/M_\odot)$	r_h (pc)	α	f_b (per cent)	β
NGC 5466	4.65	13.94	−0.97	8.0	0.00 ± 0.03
NGC 6218	4.86	4.74	−0.36	5.4	-0.24 ± 0.04
NGC 6981	4.81	7.70	−0.55	5.8	0.07 ± 0.04
NGC 6981remn	4.88	7.89	−0.55	6.4	0.09 ± 0.03
NGC 6981bin	4.78	7.59	−0.67	15.1	0.13 ± 0.02

(i) The slope of the MF α is derived by fitting the N_j coefficients with a power law. The corresponding $\mu_s(m)$ and $\mu_b(m)$ functions are calculated using equation (6).

(ii) The optimal values of ψ_0 and r_c are searched using a Markov Chain Monte Carlo algorithm maximizing the merit function defined in equation (4).

(iii) The relative fraction of stars in the eight mass bins N_i and the global binary fraction f_b are adjusted by multiplying them for corrective terms, which are proportional to the ratio between the relative number counts in each bin of the observed sample and the corresponding model prediction:

$$N'_j = N_j \left(\frac{N_j^{obs}}{N_s\, \Delta m \int_0^{R_{max}} P(m_j, R)\, dR} \right)^\eta,$$

$$f'_b = f_b \left(\frac{N_{bin}^{obs}}{N_s} \frac{\sum_{j=1}^{H} \int_0^{R_{max}} X_s(m_j, R)\, dR}{\sum_{j=1}^{H} \int_0^{R_{max}} X_b(m_j, R)\, dR} \right)^\eta,$$

where N_j^{obs} is the number of stars observed in the jth mass bin, N_{bin}^{obs} is the number of stars flagged as binaries, X_b is the same function defined in equation (5) but using the functions μ_b and C_b for the binary population, and η is a softening parameter, set to 0.5, used to avoid divergence.

The above procedure converges after ∼10 iterations providing the combination of parameter (ψ_0, r_c, N_j, f_b) corresponding to the maximum likelihood.

4 RESULTS

The parameters of the best-fitting King–Michie models are listed in Table 2 for the three analysed clusters.

The estimated masses agree within the errors, although they are slightly smaller by $\Delta\log M \sim 0.1-0.2$, with those listed by McLaughlin & van der Marel (2005). Note that these authors calculated masses by fitting the surface brightness profiles of a large sample of GCs with single-mass King (1966) models. So, some differences are expected because of the inadequacy of single-mass models to reproduce the structure of clusters with steep MF because of the significant contribution of faint low-mass stars to the total mass budget without significantly affecting the surface brightness profile (see Sollima et al. 2015).

In Fig. 4, the derived global MFs of single stars are shown. Their corresponding slopes, listed in Table 2, have been calculated by fitting a power law through the five mass bins with $m_j > 0.3\,M_\odot$. The less massive bins are indeed those which are prone to the largest systematic uncertainties (see Section 4.1) and often show a profile deviating from a power-law behaviour. The derived values of the slopes for NGC5466 and NGC6218 agree with the estimates made by Paust et al. (2010), Beccari et al. (2015) and Sollima, Bellazzini & Lee (2012) while for NGC6981 no previous estimate of the MF slope is present in the literature.

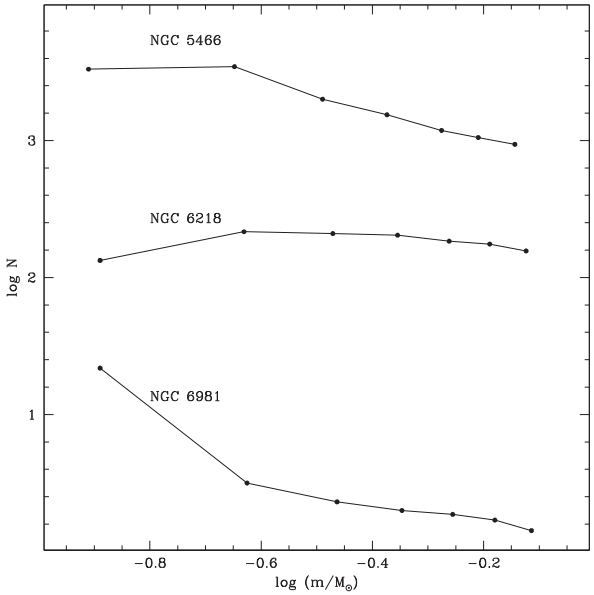

Figure 4. Modelled present-day global MFs of the three target clusters. A vertical shift has been added to each cluster for clarity.

A cluster-to-cluster comparison between the fractions of binaries estimated here and those listed in Milone et al. (2012) indicates no significant differences, although they are all systematically smaller than those estimated by these authors by $\Delta f_{\rm b} \sim 1.8$–$5.2$ per cent. Consider that the analysis of Milone et al. (2012) is conducted on the ACS field of view only, sampling the central portion of the GCs where binaries tend to sink because of mass segregation. This can explain the difference observed between these two works.

The comparison between the distribution of single stars in the m–log R plane for the three analysed clusters and the prediction of the corresponding best-fitting models is shown in Fig. 5. Qualitatively, the density contours of the models well reproduce the distribution of stars in this plane for all clusters. Another way to visualize such a comparison is shown in Fig. 6 where the completeness-corrected density profiles of stars in three different mass bins are compared with the prediction of the best-fitting models. Also in this case, the agreement is generally good. It is worth noting that the models tend to underpredict the density of all mass groups in the outermost portion of all clusters at distances $R > R_{\rm max}$. In this region, strong deviations from equilibrium are apparent as power-law tidal tails extending up to the GCs' tidal radii and beyond. This effect is particularly evident in NGC6981 where such features cover almost the entire extent of FORS2 fields.

To quantify the adequacy of models in reproducing the effect of mass segregation, we compared the cumulative radial profile of observed stars in the different mass bins $[F_j^{\rm obs}(< R)]$ with those predicted by models calculated through the relation

$$F_j^{\rm mod}(< R) = \frac{\int_0^R R\ P(m_j, R)\,{\rm d}R}{\int_0^{R_{\rm max}} R\ P(m_j, R)\,{\rm d}R}.$$

For each bin we calculated the logarithmic shift in radius $\Delta\log r_{{\rm c},j}$ to be added to the model profile to minimize the Kolmogorov–Smirnov statistic,

$${\rm KS}(m_j) = \max|F_j^{\rm obs}(< R) - F_j^{\rm mod}(< R)|.$$

The slope of the $\beta = {\rm d}\Delta\log r_{{\rm c},j}/{\rm d}\log m_j$ is then calculated and adopted as an indicator of the adequacy of the best-fitting King–Michie model in reproducing the actual degree of mass segregation. Values of β close to zero indicate a good agreement between models and observation while positive (negative) values indicate an overestimate (underestimate) of mass segregation. Note that this approach is similar to that adopted by Goldsbury et al. (2013) who quantify mass segregation in a sample of GCs using the power-law slope of the half-power radius versus mass relation. In this case, index β defined above is almost equivalent to the difference between the observed Goldsbury et al. (2013) slopes and those of the corresponding best-fitting models. The values of index β calculated for the three analysed clusters are listed in the last column of Table 2. While the values of β for NGC5466 and NGC6981 are small ($|\beta| < 0.1$), a negative value of $\beta = -0.24 \pm 0.04$ is measured for NGC6218 indicating that it is more mass segregated than what predicted by the adopted model.

4.1 Effect of assumptions

In the algorithm described in Sections 3.1 and 3.3, we adopted many assumptions. Among them, the prescription for the retention fraction of remnants and the choice of the distribution of mass ratios in binaries are arbitrary and not well constrained by observations. It is therefore important to check the actual impact of such assumptions on the results presented in Section 4. For this purpose, as a test case, we repeated the analysis for NGC6981 by assuming extreme

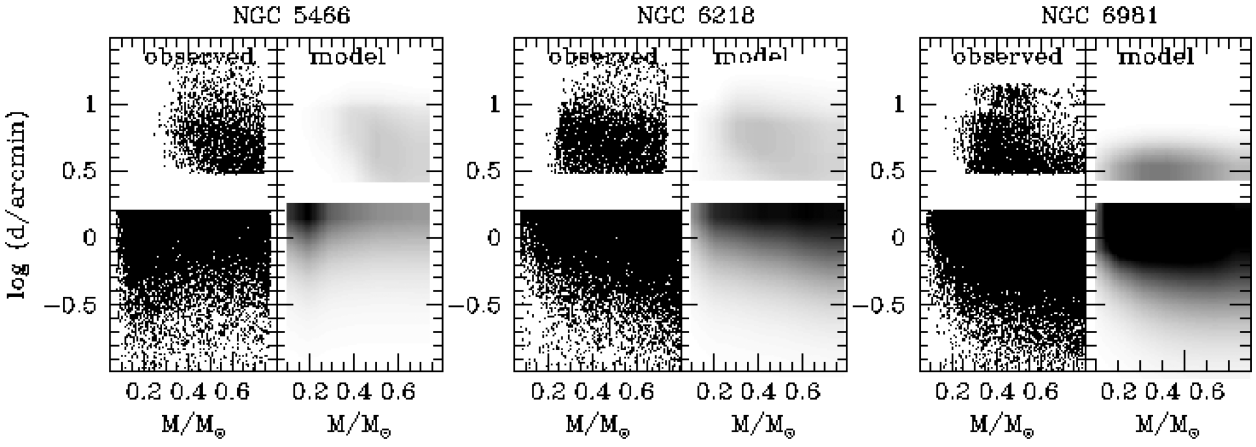

Figure 5. Distribution of single stars in the m–log R plane for the three target clusters (left panels). The probability density predicted by the best-fitting models is shown in right panels.

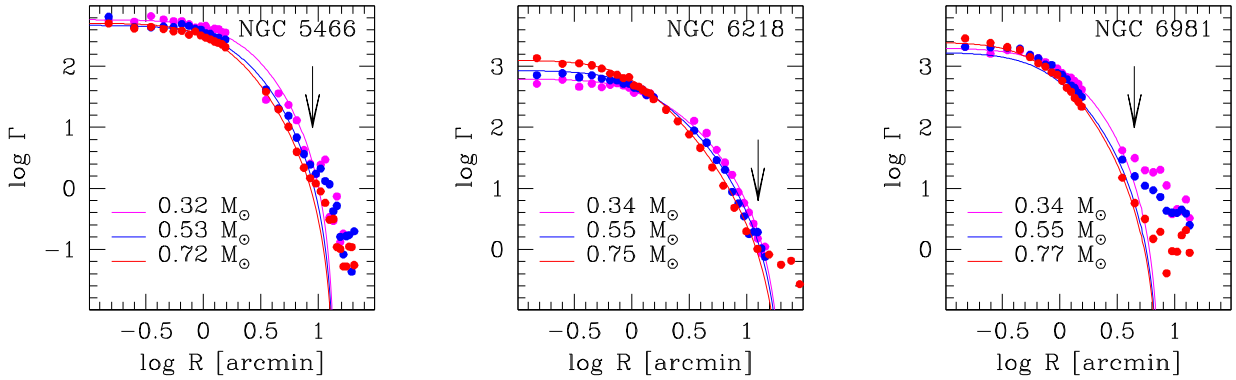

Figure 6. Completeness-corrected density profiles for different mass groups in the three target clusters. The prediction of the best-fitting King–Michie models is overplotted as solid lines. The outer limiting radii adopted in the fitting routine ($R_{\rm max}$) are marked by vertical arrows.

conditions for these parameters: (i) a 100 per cent retention of all remnants (including neutron stars and black holes with progenitor masses up to 120 $M_\odot$; named NGC6981remn in Table 2) and (ii) a mass ratio distribution of binaries drawn by randomly associating stars extracted from the MF (corresponding to a distribution peaked at $q \sim 0.3$ with a decreasing tail at large mass ratios; NGC6981bin). The resulting masses, half-mass radii, MF slopes and binary fractions are also listed in Table 2. It can be noted that masses are significantly affected only by the choice of the retention fraction of remnants, while the MF slopes and binary fractions are sensitive only to the mass ratio distribution of binaries. On the other hand, the values of β, quantifying the agreement between data and models, are shifted towards positive values. The effect of remnants on mass and size is due to the large masses of these objects with respect to single stars. So, an adopted larger fraction of remnants provides an additional mass budget which is modelled as a concentrated distribution of mass.

The large impact of the binary mass ratio distribution in the derived binary fraction and present-day MF is due to the fact that this parameter affects the classification of single and binaries (see Section 3.1). In particular, in the case of NGC6981bin, a smaller fraction of binaries is located in the binary selection box with respect to the standard assumption of a flat-mass ratio distribution. Thus, a large fraction of binaries is needed to explain the observed number of objects in this region of the CMD. Moreover, the mass ratio distribution also affects the distribution in magnitude of objects classified as binaries. As a consequence, the MF of the remaining stars classified as singles turns out to be also affected by this choice, in particular in the low-mass range. Note that the magnitude of the distortion of the MF introduced by the particular choice of the mass ratio distribution of binaries exceeds by more than an order of magnitude the statistical fluctuations due to Poisson noise.

It is interesting to note that parameter β increases with increasing the mass contained in remnants or binaries. This means that the larger is the fraction of mass contained in massive objects the larger is the degree of mass segregation predicted by multimass models, becoming larger than what observed. This occurs because a large population of massive stars increases the mass contrast with respect to the average stellar mass mimicking the effect of a steeper MF (see Section 4.2).

4.2 Comparison with *N*-body simulations

The result presented in the previous section indicates that, for the adopted recipes on the dark remnant retention fraction and the mass ratio distribution of binaries, King–Michie models well reproduce the distribution of masses in two out of three GCs analysed here while underestimating the actual degree of mass segregation in NGC6218. It is worth noting that this last cluster has the shortest half-mass relaxation time among the GCs of our sample and is therefore expected to be dynamically more evolved than the other analysed clusters. Indeed, as introduced in Section 1, mass segregation is expected to develop and grow as a result of the increasing efficiency of two-body relaxation. So, clusters in different stages of dynamical evolution are expected to be characterized by different degrees of mass segregation. It is interesting to check whether the recipe for mass segregation of multimass King–Michie models is adequate in different stages of dynamical evolution. For this purpose, we analysed different snapshots of two *N*-body simulations of star clusters in different stages of their evolution and under different initial conditions.

The *N*-body simulations considered here have been performed using the collisional *N*-body codes NBODY4 and NBODY6 (Aarseth 1999) and are part of the surveys presented by Baumgardt & Makino (2003) and Lamers, Baumgardt & Gieles (2013). Each simulation contains 131 072 particles with no primordial binaries. Particles were initially distributed following a King (1966) model with central dimensionless potential $W0 = 5$, regardless of their masses. The two simulations start with different half-mass radii (with $r_{\rm h} = 1$ and 11.5 pc, hereafter, referred to as W5rh1R8.5 and W5rh11.5R8.5, respectively). Particle masses are extracted from a Kroupa (2001) MF with a lower mass limit of 0.1 $M_\odot$ and an upper mass limit of 15 and 100 $M_\odot$, for the W5rh11.5R8.5 and W5rh1R8.5 simulations, respectively. In these configurations, the total cluster masses are 71 236.4 and 83 439 $M_\odot$ for simulations W5rh1R8.5 and W5rh11.5R8.5, respectively. The cluster moves within a logarithmic potential having circular velocity $v_{\rm circ} = 220\,{\rm km\,s^{-1}}$, on a circular orbit at a distance of 8.5 kpc from the galactic centre. The corresponding initial Jacobi radius is $r_{\rm J} = 61.15$ pc, i.e. equal to the initial tidal radius of the W5rh11.5R8.5 simulation. Because of their different Roche lobe filling factors, the tidal field affects the two simulations in extremely different ways. Moreover, the initial half-mass relaxation time is significantly longer in model W5rh11.5R8.5 ($t_{\rm rh} = 4.97$ Gyr) with respect to model W5rh1R8.5 ($t_{\rm rh} = 0.12$ Gyr). These simulations have been already used in Sollima et al. (2015) to test the bias introduced by the use of multimass King–Michie models in the estimate of mass and MF.

From these simulations we extracted snapshots at different epochs and for each of them we considered the projected positions on the *x*–*y* plane of the unevolved stars. Stars have been divided into eight

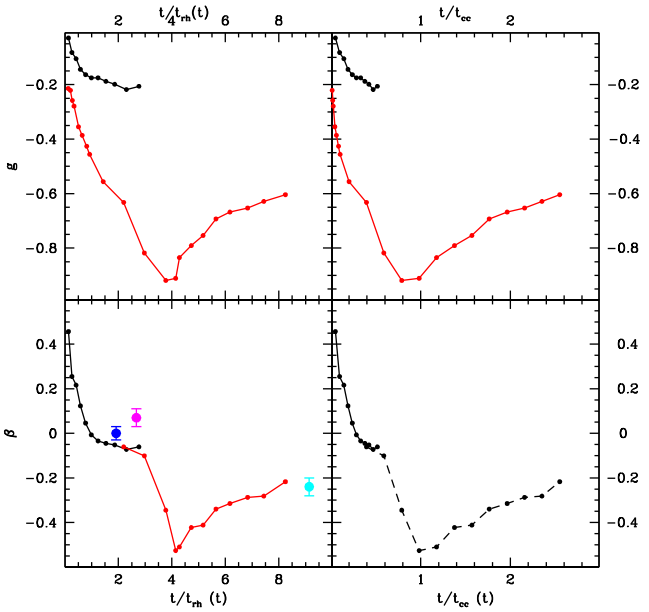

Figure 7. Time evolution of indices g (top panels) and β (bottom panels) in the two analysed N-body simulations. In left panels, time is normalized to the local half-mass relaxation time while in right panels it is normalized to the core–collapse epoch. The locations of the three target GCs in this plane are marked in the bottom-left panel as blue (NGC5466), cyan (NGC6218) and magenta (NGC6981) dots (grey dots with increasing darkness are used in the printed version of the paper).

evenly spaced mass bins and for each of them we calculated the projected radius containing half of their population. The projected half-mass radii as a function of the star mass have been then fitted with a power law whose index g (equivalent to that estimated by Goldsbury et al. 2013) gives an indication of the degree of mass segregation. The behaviour of this index as a function of time is shown in the top panels of Fig. 7. In this figure, time has been normalized to two characteristic time-scales: the half-mass relaxation time $t_{\rm rh}(t)$ (Spitzer 1987) and the core–collapse time $t_{\rm cc}$. The index g is $\sim$0 at the beginning of both simulations (as expected since simulation stars with no mass segregation) and then decreases until core collapse. A slow and steady increase of the g index is apparent in the post-core–collapse phase of simulation W5rh1R8.5. Note that the declining rate of g of simulation W5rh1R8.5 is steeper than that of simulation W5rh11.5R8.5, regardless of the time normalization. This is due to the different efficiency of two-body relaxation in producing mass segregation in the two simulations. Indeed, after the same number of half-mass relaxation times, simulation W5rh11.5R8.5 lost a significantly larger fraction of its stars with respect to simulation W5rh1R8.5 because of the strong interaction with the tidal field. Thus, it has a flatter MF while maintaining a less concentrated profile. Under these conditions, the average mass contrast in long-range interactions decreases reducing the efficiency of two-body relaxation. For the same reason, mass segregation and the radial flows of specific heat leading to core collapse proceed on different time-scales. Summarizing the behaviour of the mass segregation index g, although linked to the stage of dynamical evolution of the cluster, is highly sensitive to initial conditions like initial MF, strength of the tidal field and concentration.

For comparison, we considered the fit to the analysed snapshots made in Sollima et al. (2015) with multimass King–Michie models and calculated index β using the technique described in Section 4. The values of β are plotted in the bottom panel of Fig. 7 as a function of time. It is interesting to note that the values of β derived for the two simulations coincide in the overlap range of time. This occurs both considering the half-mass relaxation and the core–collapse time-scale for normalization. In general, four different stages can be defined in this plot:

(i) An initial phase [when $t < t_{\rm rh}(t)$] where two-body relaxation is still not effective in redistributing kinetic energies among stars with different masses. In this phase, the actual degree of mass segregation is smaller than the prediction of multimass King–Michie models still resembling the initial condition (decreasing g; $\beta > 0$).

(ii) An intermediate phase [$t_{\rm rh}(t) < t < t_{\rm cc}$] in which the system sets in an equilibrium state where its structural variations (size, mass, concentration and MF) are coupled to a progressive increase of the degree of mass segregation nicely following the prescription for kinetic energy balance predicted by King–Michie models (decreasing g; $\beta \sim 0$).

(iii) The core–collapse phase where a cusp in the central potential develops. The presence of this cusp violates the boundary condition of King–Michie models at the centre [$\mathrm{d}\psi/\mathrm{d}r(0) \neq 0$] making their prediction for mass segregation underestimated ($\beta < 0$).

(iv) The post-core–collapse phase where binaries release kinetic energy during collisions with (mainly massive) stars in the cluster core. This produces the bounce of the core and a decrease of the degree of mass segregation (increasing g and β).

Note that, while the duration of the initial phase is set by the efficiency of two-body relaxation (thus scaling with the half-mass relaxation time), the duration of the intermediate phase depends on the many parameters affecting the core–collapse epoch. In particular, the presence of a significant population of hard binaries can delay core collapse by a significant factor (Gao et al. 1991). So, although such a phase lasts at $t \sim 4\,t_{\rm rh}$ in the considered simulations (run without primordial binaries), its duration could be several Gyr long in real GCs, representing the most common among their stages of dynamical evolution. The location in this diagram of the three analysed GCs is overplotted in Fig. 7. Note that while NGC5466 and NGC6981 lie in the intermediate-phase region, the negative value of β measured in NGC6218, together with its large value of $t/t_{\rm rh}(t)$ put this cluster in the post-core–collapse phase.

5 SUMMARY

In this paper, we showed that the radial distribution of stars in three Galactic GCs is broadly consistent with the prediction of analytic King–Michie multimass models. In particular, in two of them (NGC5466 and NGC6981) we found no appreciable difference in the dependence of the characteristic radii on stellar mass. This result confirms what already found in Sollima et al. (2015), who however based their analysis on a set of N-body simulations and focused only on the accuracy in the mass and MF estimate.

In the commonly used formulation by Gunn & Griffin (1979), these models assume that the exponent in the lowered Maxwellian distribution function [see equation (1)] is directly proportional to the stellar mass. Note that, because of the tidal truncation in energy, this condition differs from kinetic energy equipartition. Indeed, the actual squared velocity dispersions of the different mass groups in this model do not follow a $\sigma \propto m^{-0.5}$ relation, neither globally nor at any radius. On the other hand, the resulting behaviour of the σ–m relation is closer to equipartition in the central region than in the outer parts. Note that the assumption made by Gunn & Griffin (1979) is arbitrary and other choices are equally justified (see e.g.

Merritt 1981). In spite of this, the results presented here show that these models provide a good representation of real GCs, although the choice of the (uncertain) recipes to account for the fraction of retained remnants and the characteristics of the binary population have significant effects. The comparison with *N*-body simulation spanning the entire evolution of a simulated star cluster under two different initial conditions indicates that this agreement is expected during a time interval between the half-mass relaxation time and the core–collapse epoch, regardless of the initial conditions. Such a time interval is expected to constitute a significant portion of the evolution of GCs, this being probably the most common stage experienced by present-day GCs. On the other hand, significant differences between King–Michie models and GCs are instead expected when the cluster is still dynamically young ($t < t_{\rm rh}$) or near and after core collapse. In this regard, parameter β, defined as the difference between the observed and predicted power-law indices of the characteristic radius–stellar mass relation, has been found to be useful in distinguishing the dynamical stage of an observed cluster, this being almost insensitive to initial conditions.

An notable case is represented by the GC NGC6218 whose massive stars appear to be significantly more segregated than what predicted by models. This is indicated by the negative value of parameter β measured in this cluster ($\beta = -0.24 \pm 0.04$) at odds with those estimated in the other three GCs of our sample ($\beta \sim 0$). Note that this cluster has a flat MF ($\alpha = -0.36$; suggesting a strong mass-loss history; de Marchi, Pulone & Paresce 2006; Sollima et al. 2012) and a short present-day half-mass relaxation time [$t_{\rm rh}(t) \sim 1.4$ Gyr]. It is therefore possible that it could have already experienced core collapse in the past.

ACKNOWLEDGEMENTS

We warmly thank the anonymous referee for his/her helpful comments and suggestions. AS acknowledges the PRIN INAF 2011 'Multiple populations in globular clusters: their role in the Galaxy assembly' (PI E. Carretta) and the PRIN INAF 2014 'Probing the internal dynamics of globular clusters. The first one is comprehensive radial mapping of individual star kinematics with the generation of multi-object spectrographs' (PI: L. Origlia). ED and CP acknowledge support from the European Research Council (ERC-2010-AdG-267675, COSMIC-LAB).

Based on FOcal Reducer and low dispersion Spectrograph (FORS) observations collected with the Very Large Telescope of the European Southern Observatory, Cerro Paranal, Chile, within the observing programmes 091.D-0562(A) and 093.D-0228(A) (PI: Dalessandro), and on observations made with the Large Binocular Camera at the Large Binocular Telescope within program INAF.D07-2010A (PI: Ferraro) and with the Advanced Camera for Surveys (ACS) on board to the NASA/ESA *Hubble Space Telescope* under programs GO-10775 (PI: Sarajedini).

REFERENCES

Aarseth S. J., 1999, PASP, 111, 1333
Albrow M. D., De Marchi G., Sahu K. C., 2002, ApJ, 579, 660
Anderson J. et al., 2008, AJ, 135, 2055
Andreuzzi G., Buonanno R., Fusi Pecci F., Iannicola G., Marconi G., 2000, A&A, 353, 944
Andreuzzi G., Testa V., Marconi G., Alcaino G., Alvarado F., Buonanno R., 2004, A&A, 425, 509
Balbinot E., Santiago B. X., Bica E., Bonatto C., 2009, MNRAS, 396, 1596
Baumgardt H., Makino J., 2003, MNRAS, 340, 227
Beccari G., Pasquato M., De Marchi G., Dalessandro E., Trenti M., Gill M., 2010, ApJ, 713, 194
Beccari G., Dalessandro E., Lanzoni B., Ferraro F. R., Sollima A., Bellazzini M., Miocchi P., 2013, ApJ, 776, 60
Beccari G., Dalessandro E., Lanzoni B., Ferraro F. R., Bellazzini M., Sollima A., 2015, ApJ, 814, 144
Belczynski K., Bulik T., Fryer C. L., Ruiter A., Valsecchi F., Vink J. S., Hurley J. R., 2010, ApJ, 714, 1217
Bellazzini M., Fusi Pecci F., Messineo M., Monaco L., Rood R. T., 2002, AJ, 123, 1509
Bellini A. et al., 2014, ApJ, 797, 115
Bolte M., 1989, ApJ, 341, 168
Carballo-Bello J. A., Gieles M., Sollima A., Koposov S., Martínez-Delgado D., Peñarrubia J., 2012, MNRAS, 419, 14
Carretta E., Bragaglia A., Gratton R., D'Orazi V., Lucatello S., 2009, A&A, 508, 695
Da Costa G. S., 1982, AJ, 87, 990
Da Costa G. S., Freeman K. C., 1976, ApJ, 206, 128
Dalessandro E., Ferraro F. R., Massari D., Lanzoni B., Miocchi P., Beccari G., 2015, ApJ, 810, 40
de Marchi G., Paresce F., 1996, ApJ, 467, 658
de Marchi G., Pulone L., Paresce F., 2006, A&A, 449, 161
Djorgovski S., 1993, in Djorgovski S. G., Meylan G., eds, ASP Conf. Ser. Vol. 50, Structure and Dynamics of Globular Clusters. Astron. Soc. Pac., San Francisco, p. 373
Dotter A., Chaboyer B., Jevremović D., Baron E., Ferguson J. W., Sarajedini A., Anderson J., 2007, AJ, 134, 376
Dotter A. et al., 2010, ApJ, 708, 698
Drukier G. A., Fahlman G. G., Richer H. B., Searle L., Thompson I., 1993, AJ, 106, 2335
Fahlman G. G., Richer H. B., Nemec J., 1991, ApJ, 380, 124
Ferraro F. R., Carretta E., Bragaglia A., Renzini A., Ortolani S., 1997, MNRAS, 286, 1012
Ferraro F. R. et al., 2012, Nature, 492, 393
Fischer P., Pryor C., Murray S., Mateo M., Richtler T., 1998, AJ, 115, 592
Frank M. J., Grebel E. K., Küpper A. H. W., 2014, MNRAS, 443, 815
Gao B., Goodman J., Cohn H., Murphy B., 1991, ApJ, 370, 567
Giersz M., 2006, MNRAS, 371, 484
Giersz M., Heggie D. C., 2009, MNRAS, 395, 1173
Giersz M., Heggie D. C., 2011, MNRAS, 410, 2698
Giersz M., Heggie D. C., Hurley J. R., 2008, MNRAS, 388, 429
Goldsbury R., Heyl J., Richer H., 2013, ApJ, 778, 57
Gunn J. E., Griffin R. F., 1979, AJ, 84, 752
Harfst S., Portegies Zwart S., Stolte A., 2010, MNRAS, 409, 628
Harris W. E., 1996, AJ, 112, 1487
Heggie D. C., 2014, MNRAS, 445, 3435
Hurley J. R., Pols O. R., Aarseth S. J., Tout C. A., 2005, MNRAS, 363, 293
Inagaki S., Saslaw W. C., 1985, ApJ, 292, 339
Irwin M. J., Trimble V., 1984, AJ, 89, 83
Johnston K. V., Sigurdsson S., Hernquist L., 1999, MNRAS, 302, 771
Kamann S. et al., 2016, A&A, 588, A149
King I. R., 1966, AJ, 71, 64
King I. R., Sosin C., Cool A. M., 1995, ApJ, 452, L33
Koch A., Grebel E. K., Odenkirchen M., Martínez-Delgado D., Caldwell J. A. R., 2004, AJ, 128, 2274
Kroupa P., 2001, MNRAS, 322, 231
Kruijssen J. M. D., 2009, A&A, 507, 1409
Küpper A. H. W., Kroupa P., Baumgardt H., Heggie D. C., 2010, MNRAS, 407, 2241
Lamers H. J. G. L. M., Baumgardt H., Gieles M., 2013, MNRAS, 433, 1378
Lee K. H., Lee H. M., Fahlman G. G., Lee M. G., 2003, AJ, 126, 815
Lee K. H., Lee H. M., Fahlman G. G., Sung H., 2004, AJ, 128, 2838
Martinazzi E., Pieres A., Kepler S. O., Costa J. E. S., Bonatto C., Bica E., 2014, MNRAS, 442, 3105
McLaughlin D. E., van der Marel R. P., 2005, ApJS, 161, 304
Merritt D., 1981, AJ, 86, 318
Milone A. P. et al., 2012, A&A, 540, A16
Miocchi P. et al., 2013, ApJ, 774, 151

Paresce F., de Marchi G., Jedrzejewski R., 1995, ApJ, 442, L57
Pasquali A., De Marchi G., Pulone L., Brigas M. S., 2004, A&A, 428, 469
Pasquato M., Trenti M., De Marchi G., Gill M., Hamilton D. P., Miller M. C., Stiavelli M., van der Marel R. P., 2009, ApJ, 699, 1511
Paust N. E. Q. et al., 2010, AJ, 139, 476
Pryor C., Smith G. H., McClure R. D., 1986, AJ, 92, 1358
Richer H. B., Fahlman G. G., 1989, ApJ, 339, 178
Richer H. B., Fahlman G. G., Vandenberg D. A., 1988, ApJ, 329, 187
Richer H. B. et al., 2004, AJ, 127, 2771
Robin A. C., Reylé C., Derrière S., Picaud S., 2003, A&A, 409, 523
Rood R. T. et al., 1999, ApJ, 523, 752
Rosenberg A., Saviane I., Piotto G., Aparicio A., Zaggia S. R., 1998, AJ, 115, 648
Sarajedini A. et al., 2007, AJ, 133, 1658
Saviane I., Piotto G., Fagotto F., Zaggia S., Capaccioli M., Aparicio A., 1998, A&A, 333, 479
Sirianni M. et al., 2005, PASP, 117, 1049
Skrutskie M. F. et al., 2006, AJ, 131, 1163
Sollima A., Bellazzini M., Lee J.-W., 2012, ApJ, 755, 156
Sollima A., Baumgardt H., Zocchi A., Balbinot E., Gieles M., Hénault-Brunet V., Varri A. L., 2015, MNRAS, 451, 2185
Sosin C., 1997, AJ, 114, 1517
Spitzer L., 1987, Dynamical Evolution of Globular Clusters. Princeton Univ. Press, Princeton, NJ
Stetson P. B., 1994, PASP, 106, 250
Takahashi K., Lee H. M., 2000, MNRAS, 316, 671
Testa V., Zaggia S. R., Andreon S., Longo G., Scaramella R., Djorgovski S. G., de Carvalho R., 2000, A&A, 356, 127
Trenti M., van der Marel R., 2013, MNRAS, 435, 3272
Wang L. et al., 2016, MNRAS, 458, 1450
Watkins L. L., van der Marel R. P., Bellini A., Anderson J., 2015, ApJ, 803, 29
Zaggia S. R., Piotto G., Capaccioli M., 1997, A&A, 327, 1004
Zhang C. et al., 2015, ApJ, 815, 95
Zonoozi A. H., Küpper A. H. W., Baumgardt H., Haghi H., Kroupa P., Hilker M., 2011, MNRAS, 411, 1989
Zonoozi A. H., Haghi H., Küpper A. H. W., Baumgardt H., Frank M. J., Kroupa P., 2014, MNRAS, 440, 3172

This paper has been typeset from a TEX/LATEX file prepared by the author.